www.MaterialsViews.com

ADVANCED
FUNCTIONAL
MATERIALS
www.afm-journal.de

FULL PAPER

NiO_X/MoO_3 Bi-Layers as Efficient Hole Extraction Contacts in Organic Solar Cells

Philip Schulz,* Sarah R. Cowan, Ze-Lei Guan, Andres Garcia, Dana C. Olson, and Antoine Kahn

The electronic structure of a bi-layer hole extraction contact consisting of nickel oxide (NiO_x) and molybdenum trioxide (MoO_3) is determined via ultraviolet and X-ray photoemission spectroscopy. The bi-layer presents ideal energetics for the extraction of holes and suppression of carrier recombination at the interface. The application of the NiO_x/MoO_3 bi-layer as the anode of organic bulk heterojunction solar cells based on PCDTBT/PC_{71}BM leads to improved device performance, which is explained by an intricate charge transfer process across the interface.

1. Introduction

Organic photovoltaic (OPV) cells based on small molecule and polymer donor and acceptor materials have spurred much interest in research and development in the last two decades, because of their potential for large-area-scalable and flexible applications. Although significant progress has been recently reported for a 12% power conversion efficiency (PCE) in evaporated small molecule cells[1] and a 10.6% PCE in polymer multi-junction cells,[2] further performance enhancement and device stability are required in order to open a path toward commercialization.[1,3,4] Blends of polymers and small molecules have been identified as versatile systems for the realization of inexpensive and high performance solar cells.[5–7] Yet, improvements to device characteristics have been made primarily by the development of improved absorber materials in the active layer. The open circuit voltage (V_{OC}) is maximized by employing acceptor molecules with low electron affinity (EA) and hole-conducting donor polymers with high ionization energy (IE).[6–10] However, the latter brings the challenge of the choice of anode, as the deep-lying highest occupied molecular orbital (HOMO) of the polymer requires a similarly high work function contact in order to allow efficient harvesting of holes. Recently, solution-processed devices were demonstrated with either high work function metal oxides, such as molybdenum oxide (MoO_3) or the conducting polymer poly(3,4-ethylenedioxythiophene):poly-(styrenesulfonate) (PEDOT:PSS).[3,11–13] However, the hygroscopic and acidic nature of PEDOT:PSS raises some issues concerning lower overall performance and stability.[14–17] An additional important requirement for the hole-collecting contact is to block the electrons from the acceptor material in order to avoid undesirable recombination at the interface. Metal oxides with low electron affinity, such as nickel oxide (NiO_x), have been identified as prospective candidates.[18,19] Yet, the work function and ionization energy of as-deposited NiO_x is often too low for the newest generation of hole-conducting donor polymers such as poly[[9-(1-octylnonyl)-9H-carbazole-2,7-diyl]-2,5-thiophenediyl-2,1,3-benzothiadiazole-4,7-diyl-2,5-thiophenediyl] (PCDTBT) and small molecules such as 5,5′-bis{7-(4-(5-hexylthiophen-2-yl)thiophen-2-yl)-[1,2,5]thiadiazolo[3,4-c]pyridine}-3,3′-di-2-ethylhexylsilylene-2,2′ bithiophene (d-DTS-$(PTTh_2)_2$), thereby leading to an energy loss in the hole extraction process.[14] It was previously shown that surface treatment with an O_2 plasma can reduce this barrier, resulting in dramatic increases in device performance.[18–20] Here, we present an alternate approach, where the electron blocking properties of NiO_x are combined with the hole extracting capabilities of MoO_3 to enhance the efficiency of hole harvesting at the anode. The electronic structure of these oxide films was previously investigated, and MoO_3[21–24] was found to be a very high work function n-type oxide, doped by oxygen vacancies, while NiO_x is one of the few p-type oxides, with Ni vacancies acting as p-type dopants.[25] Energy level alignment and charge recombination mechanisms at this, and other, oxide/oxide interfaces remain somewhat unclear in spite of several previous investigations of the energy levels and electronic parameters of these individual materials.[19,23] Furthermore, MoO_3 by itself has recently been shown not to be an electron blocking layer due to its very deep conduction band minimum (very large electron affinity of ≈6.7 eV for vacuum deposited films).[26] One of the issues addressed in this work is therefore whether a very thin layer of MoO_3 can improve the NiO_x contact by increasing its work function without providing a detrimental pathway for electron recombination.

Dr. P. Schulz, Dr. Z.-L. Guan, Prof. A. Kahn
Department of Electrical Engineering
Princeton University
Princeton, NJ, 08544, USA
Dr. S. R. Cowan, Dr. A. Garcia, Dr. D. C. Olson
National Renewable Energy Laboratory
National Center for Photovoltaics
Golden, CO, 80401, USA
E-mail: phschulz@princeton.edu

**ADVANCED
FUNCTIONAL
MATERIALS**

www.afm-journal.de

Materials Views

www.MaterialsViews.com

FULL PAPER
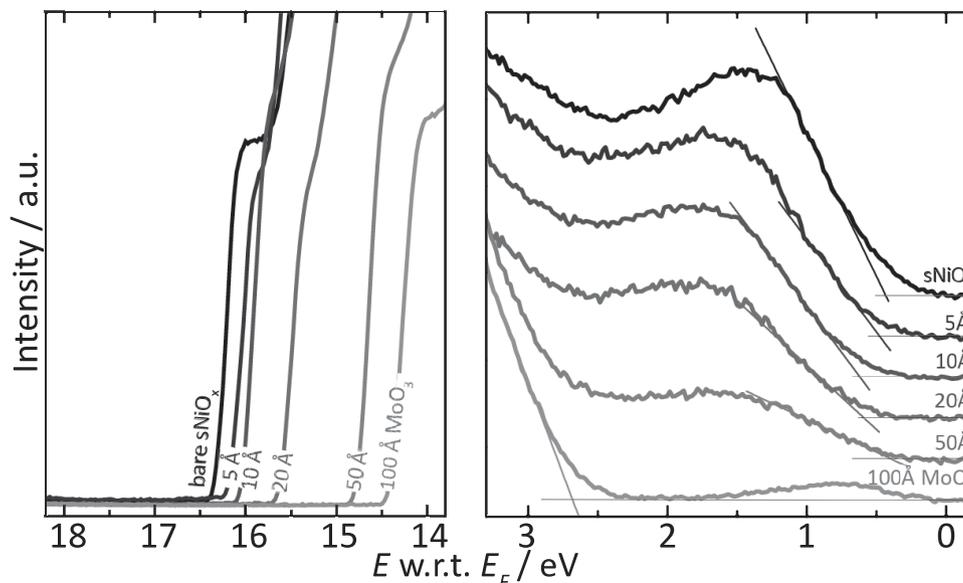
Figure 1. UPS spectra of bare sNiO$_x$ and sNiO$_x$ with incrementally deposited MoO$_3$ layer (5, 10, 20, 50, and 100 Å) on top. Work functions measured from the photoemission cutoff in the He I spectra amount to 4.7, 4.9, 5.0, 5.4, 6.2 and 6.6 eV, respectively. The valence band spectra depicted on the right hand side are taken at He II excitation. The emergence of the MoO$_3$ surface state is clearly observed for a thickness of 100 Å.

2. Electronic Structure

Figure 1 shows ultra-violet photoemission spectra (UPS) of the solution processed nickel oxide (sNiO$_x$) film with an incrementally deposited top layer of MoO$_3$ (5 to 100 Å). The photoemission cutoff is used here to determine the position of the vacuum level and the work function of the film, using the pre-determined position of the Fermi level of the sample and following a well-established procedure.[27] The sNiO$_x$ film has a work function of 4.7 eV and the Fermi level (E_F) at 0.5 eV above the valence band edge, in good agreement with previous measurements done in our group. These numbers indicate that sNiO$_x$ is p-doped, a result of the presence of nickel vacancies in the film. In contrast, evaporated nickel oxide films have a larger density of oxygen vacancies, which act as donors and tend to somewhat compensate the p-doping.[18] The deposition of MoO$_3$ leads to a large shift of the photoemission cutoff indicative of an upward movement of the vacuum level and a corresponding increase in work function. This is due to an electron transfer from sNiO$_x$ to MoO$_3$ with formation of an interface dipole between the two materials, consistent with the formation of a MoO$_3$ film with a large work function of 6.8 eV. The right panel of Figure 1 displays the He II spectra of the density of states near the valence band maximum (VBM). The bare sNiO$_x$ VBM is at ≈0.5 eV below E_F and the ionization energy (IE) of the material is 5.2 eV. The 3.2 eV band gap of sNiO$_x$[19] places the conduction band minimum (CBM) at 2.6 eV above E_F, corresponding to an electron affinity (EA) of 2.1 eV, and justifying the role of this oxide as an electron-blocker. With the deposition of MoO$_3$, the sNiO$_x$ valence band exhibits both energy shifts and intensity reduction but no significant additional features. The valence band onset remains determined by the Ni 3d bands. At a MoO$_3$ thickness beyond 20 Å, the Mo 4d level

becomes apparent with an onset at a binding energy of ≈3 eV. The final position of the MoO$_3$ VBM is 2.7 eV below E_F for the 100 Å thick film. Given the 6.6 eV work function, the IE of the film is 9.3 eV. The combination of UPS and inverse photoemission spectroscopy has previously shown an energy gap of 3.0 eV for MoO$_3$.[21–23] Using this value, we obtain an EA of 6.3 eV and a conduction band minimum positioned at 0.3 eV above E_F, in good agreement with previous measurements.[21,22,26] In addition, a significant density of states is seen in the direct vicinity of the Fermi level on the 100 Å thick MoO$_3$ film. These gap states have been reported earlier for clean evaporated MoO$_3$ surfaces.[13] The existence of these gap states for the MoO$_3$ films with lower thickness cannot be excluded. However, the features in this spectral region would be screened in the UPS spectra by the Ni 3d level.

To complete the energy diagram of the interface, X-ray photoemission spectroscopy (XPS) core level spectra of the Ni 2p and Mo 3d are measured in order to identify peak shifts associated with band bending in either material. As expected, the intensity of the Ni 2p decreases and that of the Mo 3d peak increases with incremental MoO$_3$ deposition (**Figure 2**). The Ni 2p peak exhibits a 0.2–0.3 eV shift toward lower binding energy, suggesting a slight upward band bending. On the other side of the interface, the Mo 3d peak shows a shift of similar magnitude in the same direction, indicating that the interface Mo species exhibit higher binding energy. Therefore downward band bending is assumed for the MoO$_3$ at the interface to the sNiO$_x$ layer. In total this yields a classical picture of static charge transfer across the oxide junction, which can be described by the MoO$_3$ effectively doping the sNiO$_x$. In a recombination process, electrons from the MoO$_3$ conduction band drop into the valence band of the adjacent sNiO$_x$. The resulting space charge zone leads to the 0.2–0.3 eV band bending on both sides of
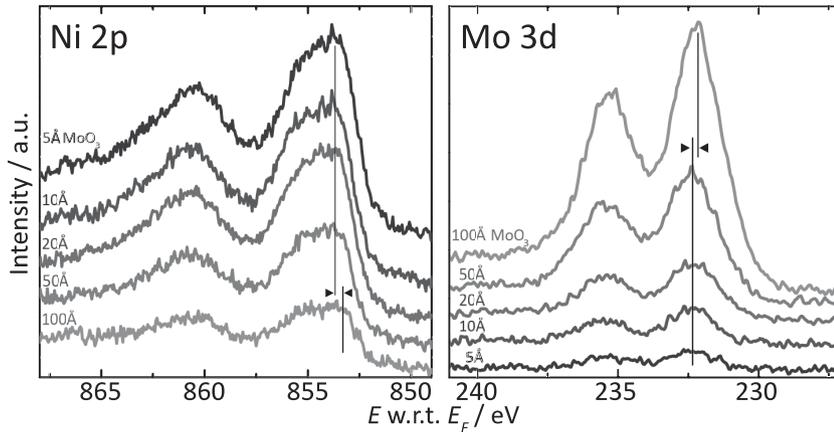
Figure 2. XPS spectra of sNiO$_x$ with incrementally deposited MoO$_3$ layer (5, 10, 20, 50, and 100 Å) on top. Ni 2p core level spectra show a 0.2–0.3 eV shift towards lower binding energy with increasing MoO$_3$ thickness indicating upwards band bending. Mo 3d core level spectra show an equally incisive shift in the same direction indicating that the Mo species at the interface undergo downwards band bending.

the interface. As a consequence, the small barrier for charge transfer from the nickel oxide valence band to the molybdenum oxide conduction band is further lowered. The complete band diagram is depicted in **Figure 3**a, underlining the close proximity of the CBM of MoO$_3$ and VBM of sNiO$_x$.

To test for electrical transport across the interface, current density versus voltage (J–V) characteristics were obtained on a structure consisting of 50 nm MoO3 deposited on 25 nm sNiO$_x$ on indium tin oxide (ITO) (Figure 3b). Two different charge transport mechanisms, depicted in Figure 3c, can be suggested based on the band diagram derived from the photoemission experiments. At negative bias on the MoO$_3$ side, electrons are injected from the cathode to the CBM of MoO$_3$ and recombine

at the MoO$_3$/sNiO$_x$ interface with holes injected from the anode to the valence band of sNiO$_x$. At positive bias, electrons and holes are generated at the MoO$_3$/sNiO$_x$ interface by electron injection from the sNiO$_x$ VBM to the MoO$_3$ CBM, drift in opposite directions and are collected at the electrodes. Both mechanisms lead to relatively good conduction through the bi-layer system, as seen from net current densities on the order of 0.01 mA cm^{-2} at an electric field of ≈0.5 MV cm^{-1}. The symmetry of the curve indicates that both processes, in forward and reverse bias, are equally efficient.

3. OPV Device Performance

The J–V characteristics of PCDTBT/PC$_{71}$BM BHJ solar cells under illumination with hole collecting interlayer/anode consisting of bare sNiO$_x$, bare MoO$_3$, or a sNiO$_x$/MoO$_3$ bilayer, with varied evaporated MoO$_3$ thickness, on ITO are given in **Figure 4**a. Figure 4b shows the dark current corresponding to these different device architectures. Each J–V curve shown here is an average obtained from 2–4 devices per substrate. Under illumination, the short circuit current density (J$_{SC}$) is roughly similar for all devices, corresponding to similar photoabsorption in the BHJ active layer for the device series, with slightly varying extraction efficiency.

EQE data and simulation via transfer matrix method, given in Supporting Information, Figure S6, demonstrate that the PCDTBT/PC$_{71}$BM cells fulfill their intended functionality and all yield steady and reproducible device characteristics throughout the whole sample series. This includes the fact that the EQE profiles are in accordance to earlier measurements on PCDTBT/PC$_{71}$BM cells with alternate anode materials such as PEDOT:PSS and ITO but also sNiO$_x$.[17] The quasi-identity of all the EQE curves, in comparison to optically modeled maximum absorption, means that any change in the device performance cannot be attributed to changes in the functionality of the bulk heterojunction itself, but must be related to optical and electrical phenomena occurring at the interface with the underlying hole extraction layer.

Indeed, it becomes apparent from the J–V characteristics under illumination that the device performance changes with the interlayer. As expected, the untreated sol-gel NiO$_x$ layer yields inferior results. The low device efficiency of 2.5% is primarily due to the mediocre fill factor (FF = 44%) and low open circuit voltage (V$_{OC}$ = 530 mV). Since the work function of the sNiO$_x$ layer is lower than the PCDTBT ionization energy, the built-in potential is reduced. The barrier for

Figure 3. a) Schematic energy level alignment of the sNiO$_x$/MoO$_3$ interface, showing a vanishing energetic barrier for charge transfer. b) I–V characteristic for a bi-layer of 25 nm sNiO$_x$ and 50 nm MoO$_3$ exhibit a symmetric curve progression. c) Schematic view on the charge transport processes involved. Forward bias leads to a recombination at the interface, whereas reverse bias results in charge generation. Both scenarios yield similar net current densities.

ADVANCED
FUNCTIONAL
MATERIALS
www.afm-journal.de

Materials
Views
www.MaterialsViews.com

Figure 4. OPV device characteristics. a) *J–V* curves under illumination show a clear diode characteristic for all tested devices. The inset depicts a close-up of the area relevant for device operation and reveals a significant increase of V_{OC} for the transition from bare sNiO$_x$ to MoO$_3$ covered surfaces. b) *J–V* curves without illumination show smaller dark currents for the devices with the bi-layer anode indicating improved electron blocking.

hole transfer from the PCDTBT HOMO to the oxide VBM leads to an increase in recombination, thus diminishing the overall voltage gain in the heterojunction. In contrast, the bare MoO$_3$ on ITO improves the device characteristics significantly. With the increase of the work function and reduction of the barrier for hole extraction, V_{OC} increases by over 300 mV to 836 mV and the efficiency is almost doubled to 4.75%, which is also improved with an 11% increase in FF to 55%.

However, two processes can be identified for the transition to the bi-layer hole contact, which become apparent with increasing MoO$_3$ film thickness. First, the open circuit voltage shows a dramatic initial jump to 871 mV with only 5 Å of MoO$_3$ and reaches 888 mV for the maximum MoO$_3$ film thickness of 100 Å on sNiO$_x$. We conclude that the increase in work function with the very first layer of MoO$_3$ on sNiO$_x$ and the concomitant doping of the sNiO$_x$ by MoO$_3$ result in an effective reduction of the extraction barrier for holes. This leads to a reduction in recombination at the interface. Second, the fill factor exhibits a gradual increase with MoO$_3$ thickness. We observe that this increment of the fill factor scales approximately with the work function increase of the bi-layer surface. This relation is in accordance to theoretical models on OPV functionality where the built-in field of the solar cell is a function of the work function difference at the contacts.[28] Though further increases in V_{OC} with MoO$_3$ film thickness are marginal, the resistance at V_{OC} is greatly reduced at the contact interfaces as the increased built-in field enhances the collection of charge carriers from the bulk. This effect is strongest for voltages close to V_{OC}, where for finite surface recombination velocities the impact of non-Ohmic contacts on the current density is most pronounced.[29] Thereby the slope of the *J–V* curve at V_{OC} becomes steeper for a higher built-in field and consequently the fill factor increases.

We find that the sNiO$_x$/MoO$_3$ bi-layer serves two complementary purposes. First, holes are efficiently extracted due to the reduced barrier and recombination at the doped sNiO$_x$

layer, leading to an immediate increase in V_{OC}. Second, the further increase in the work function for thicker MoO$_3$ films leads to a larger build-in electric field at V_{OC} and hence a more ideal diode characteristic of the solar cell. Changes in the optical properties of the bulk heterojunction, which could impact J_{SC}, can be ruled out from the EQE curves together with transfer matrix modeling (see supplement). Though these effects are already clearly visible for a bare MoO$_3$ hole extraction layer, the bi-layer structure increases the open circuit voltage by another 50 mV due to a suppressed recombination at the interface. This finding is further supported by the dark current curves in Figure 4b. The dark current in the bi-layer device (sNiO$_x$/MoO$_3$ (10 nm)) is about one order of magnitude lower than in the device with the 10 nm MoO$_3$ hole extraction layer. This indicates that the sNiO$_x$ assists in blocking electrons at the anode of the device. Eventually, the transition to the bi-layer from the bare MoO$_3$ contact improves the device efficiency to 5.60%.

Moreover, in Figure 4b shunt resistance, R_{sh}, which is inversely proportional to leakage current, is another indication for the electron blocking capabilities of the bi-layer. Diode leakage current arises from alternative current paths across the active layer. In a mixed BHJ, acceptor and donor materials are both in contact with both anode and cathode, providing many leakage pathways.

R_{sh} is lowest in the two devices with thinnest hole extraction layer (HEL), and roughly increases with increasing HEL thickness. As the MoO$_3$ thickness increases, the HEL contact WF increases and its Fermi level moves away from the PC$_{71}$BM electron transport level, leading to a maximum efficiency as a contact when the WF matches best the PCDTBT ionization energy ≈5.5 eV. This coincides with a significant increase in shunt resistance (see Supporting Information, Table S3). Hence, we conclude that the leakage current observed in Figure 4 is very possibly related to the HEL WF, that is, to the relative positions of the HEL Fermi level and the transport levels of the active layer.

Makerials
Views
www.MaterialsViews.com

ADVANCED
FUNCTIONAL
MATERIALS
www.afm-journal.de

FULL PAPER

Table 1. Specific characteristics of device performance extracted from J–V and EQE measurements presented in Figure 4. Ionization energies (I.E.) and work functions (WF) taken from photoemission spectroscopy data (PES) presented in Figure 1

Hole extraction layer	PES data		Device data					
	I.E. [eV]	WF [eV]	J_{SC} [mA cm^{-2}]	V_{OC} [V]	PCE [%]	FF [%]	R_S [Ω cm^{-2}]	n
sNiO$_x$ (6 nm)	5.2	4.7	10.50	0.528	2.45	44.2	4.0	1.93
sNiO$_x$/MoO$_3$ (0.5 nm)	5.4	4.9	11.04	0.871	4.52	47.1	6.9	1.67
sNiO$_x$/MoO$_3$ (1.0 nm)	5.6	5.0	11.13	0.867	4.86	50.4	3.6	1.43
sNiO$_x$/MoO$_3$ (2.0 nm)	6.0	5.4	11.20	0.878	5.60	57.0	2.5	1.45
sNiO$_x$/MoO$_3$ (5.0 nm)	6.7	6.2	11.07	0.886	5.44	55.5	5.6	1.49
sNiO$_x$/MoO$_3$ (10.0 nm)	9.3	6.6	11.10	0.888	5.48	55.6	4.9	1.42
MoO$_3$ (10.0 nm)	9.6	6.8	10.30	0.836	4.75	55.2	4.0	1.42

As a further figure of merit for evaluating the bilayer sNiO$_x$/MoO$_3$ HEL contacted organic solar cells, established procedures[30] are used to fit the diode ideality factor. Ideality factor values are enumerated in **Table 1**. Dark ideality factor for the bare sNiO$_x$ substrate (n = 1.93) is significantly higher than for the bare MoO$_3$ (n = 1.42), correlating to a significantly lower power conversion efficiency with the sNiO$_x$ contact when compared to the MoO$_3$-only HEL. Dark ideality factor further corresponds to the barrier for hole transfer from the PCDTBT HOMO to the oxide VBM, as it is a measure of the efficiency of charge extraction and injection at voltages near the open circuit voltage. Near the open circuit voltage, energy offsets at the diode interfaces can reduce extraction potential and cause significant space–charge effects and recombination due to the low extraction field. With increasing thickness of MoO$_3$ at the sNiO$_x$–BHJ interface, the dark ideality factor and recombination at the contact interface decrease in functioning devices. Hence, improvement in device performance can be attributed to reduced recombination as contact work function increases and the barrier for hole extraction decreases.

4. Conclusion

In summary, the energy level alignment of the interface between evaporated MoO$_3$ and solution-processed sNiO$_x$ is determined. The bi-layer is characterized by a small energy barrier between the MoO$_3$ CBM and the sNiO$_x$ VBM, which allows for efficient charge transfer at the interface. This new bi-layer anode combines the hole extraction and electron blocking capabilities of both constituents. OPV devices built on this bi-layer show superior performance compared to devices built on single layers of these two oxides. This performance enhancement can be explained by the combination of a high built-in field due to the work function of the MoO$_3$, reduced recombination due to the doping of sNiO$_x$ by MoO$_3$ and effective electron blocking due to the sNiO$_x$. Further studies will evaluate and test the performance of other metal oxide bilayer interfaces, in particular all-solution processed bilayers, with a goal of scalability and cost-effectiveness for organic devices.

5. Experimental Section

We use a combination of ultraviolet and X-ray photoemission spectroscopy (UPS, XPS) as well as J–V measurements to determine the electronic structure and electrical behavior of interfaces of interest. We show that the combination of these materials in the bi-layer leads to a very intricate electronic structure, with a close alignment between the valence band of the electron blocking sNiO$_x$ and the conduction band of the high work function MoO$_3$. As a consequence, the investigated devices based on PCDTBT:PC$_{71}$BM show superior performance as compared to reference devices with either individual sNiO$_x$ or MoO$_3$ hole extraction layers.

In this work, sNiO$_x$ was deposited on ITO from a nickel formate precursor, as previously described.[20] All sNiO$_x$ films were deposited at NREL and shipped to Princeton under nitrogen atmosphere for analysis and for MoO$_3$ deposition for interface formation. The sNiO$_x$ films were deposited onto ITO substrates after 30 min of ultrasonic cleaning in acetone followed by isopropyl alcohol. Substrates were UV ozone-cleaned immediately prior to interlayer deposition for 60 min. Sol–gel nickel oxide films were synthesized by spin-coating the diluted nickel precursor ink at 4000 rpm for 60 s followed by annealing on a hot plate in air at 300 °C for 1 h, resulting in approximately 6 nm thick films as measured by ellipsometry and stylus profilometry.[17]

The samples made for UPS and XPS analysis were introduced in the MoO$_3$ growth chamber as-received from NREL. MoO$_3$ films were vacuum deposited from a Knudsen cell (99.99% powder, Sigma-Aldrich) and incrementally grown on sNiO$_x$ at a rate of about 0.2 Å s^{-1}. The films were then transferred to an analysis chamber under ultra-high vacuum UHV (≈10^{-10} Torr). UPS was done with He I (21.22 eV) and He II (40.8 eV) radiation lines from a discharge lamp, with a resolution of 0.15 eV. XPS was performed using the Al Kα (1486.6 eV) photon line to measure the Ni 2p, Mo 3d, and O 1s core levels to evaluate any chemistry and assist in the determination of band bending at interfaces. Current density-voltage (J–V) measurements on the sNiO$_x$/MoO$_3$ bilayer films were done using a mercury-probe station placed in nitrogen, to establish a top contact, and a semiconductor parameter analyzer (HP 4155 A). The voltage was swept from 0 V to ± 4 V with the bottom ITO anode grounded.

For devices, the sNiO$_x$ films were deposited onto commercially patterned ITO (≈10 Ω sq^{-1}, Thin Film Devices, Inc.) according to the sequence of fabrication given above. After annealing, sNiO$_x$ interlayers were loaded into a thermal evaporator for MoO$_3$ deposition. MoO$_3$ was vacuum deposited (powder, Molybdenum(VI) oxide, Sigma Aldrich, 99.98%) at 1 × 10^{-7} Torr and a rate of 0.1–0.2 Å s^{-1}. MoO$_3$ thickness was confirmed for thicker films via stylus profilometry. PCDTBT (Konarka) and PC$_{71}$BM (Nano-C) were used as received for the active layer. Anhydrous 1,2-dichlorobenzene and chlorobenzene (Aldrich) were used as received in an inert N$_2$ environment. Films of PCDTBT:PC$_{71}$BM

FULL PAPER

blend: (7 mg PCDTBT/mL; 28 mg PC$_{71}$BM/mL), were spun from 60 °C anhydrous 1,2-dichlorobenzene:chlorobenzene (3:1) blend solutions at 4500 rpm for 40 s onto the interlayers on ITO-coated glass substrates. Substrates were then annealed at 70 °C for 10 min.

To construct devices, the glass/ITO/HTL/BHJ layers were completed by the evaporation of Ca/Al top-contacts. Calcium and aluminum were evaporated in an Angstrom Engineering evaporator system, with a base pressure of 2×10^{-8} Torr, and an evaporation pressure of $3-4 \times 10^{-8}$ Torr at 0.2 Å s^{-1} for 20 nm of calcium, and 1.0 Å s^{-1} for 100 nm of aluminum. Device testing was carried out under standard 1 sun, AM1.5G test conditions using a solar simulator (Xenon lamp with a calibrated mismatch factor of 1.1 compared with the AM1.5G solar spectrum for PCDTBT:PC$_{71}$BM). Intensity calibrated to near 1-sun AM1.5G intensity via an NREL-calibrated Si solar cell. Contact was made to both the ITO and Al electrodes, from which voltage was sourced and the resulting current was measured. J_{SC} was calculated based on measured device areas of 0.11 cm^2. The series resistance (R_s) was calculated at 1.2 V. Quantum efficiency measurements were performed on a Newport Oriel IQE-200 system with a 150W Xenon arc lamp, from $\lambda = 300-800$ nm with a 5 nm step size. EQE integrated to estimate J_{SC} confirms current density measured via the solar simulator within 2%.

Supporting Information

Supporting Information is available from the Wiley Online Library or from the author.

Acknowledgements

[1] http://www.heliatek.com/wp-content/uploads/2013/01/130116_PR_Heliatek_achieves_record_cell_effiency_for_OPV.pdf (accessed: 04 November 2013).

[2] J. You, L. Dou, K. Yoshimura, T. Kato, K. Ohya, T. Moriarty, K. Emery, C. C. Chen, J. Gao, G. Li, Y. Yang, *Nat. Commun.* **2013**, *4*, 1446.

[3] J. Y. Kim, K. Lee, N. E. Coates, D. Moses, T.-Q. Nguyen, M. Dante, A. J. Heeger, *Science* **2007**, *317*, 222.

[4] T. Ameri, G. Dennler, C. Lungenschmied, C. J. Brabec, *Energy Environ. Sci.* **2009**, *2*, 347.

[5] Y. Liang, Z. Xu, J. Xia, S.-T. Tsai, J. Wu, G. Li, C. Ray, L. Yu, *Adv. Mater.* **2010**, *22*, E13.

[6] S. H. Park, A Roy, S. Beaupré, S. Cho, N. Coates, J. S. Moon, D. Moses, M. Leclerc, K. Lee, A. J. Heeger, *Nat. Photonics* **2009**, *3*, 297.

[7] T. S. van der Poll, J. A. Love, T.-Q. Nguyen, G. C. Bazan, *Adv. Mater.* **2012**, *24*, 3646.

[8] He, Y., H.-Y. Chen, J. Hou, Y. Li, *J. Am. Chem. Soc.* **2010**, *132*, 1377.

[9] N. Blouin, A. Michaud, D. Gendron, S. Wakim, E. Blair, R. Neagu-Plesu, M. Belletête, G. Durocher, Y. Tao, M. Leclerc, *J. Am. Chem. Soc.* **2008**, *130*, 732.

[10] C. Piliego, T. W. Holcombe, J. D. Douglas, C. H. Woo, P. M. Beaujuge, J. M. J. Fréchet, *J. Am. Chem. Soc.* **2010**, *132*, 7595.

[11] S. Sista, M.-H. Park, Z. Hong, Y. Wu, J. Hou, W. L. Kwan, G. Li, Y. Yang, *Adv. Mater.* **2010**, *22*, 380.

[12] J. Gilot, M. M. Wienk, R. A. Janssen, *Appl. Phys. Lett.* **2007**, *90*, 143512.

[13] S. R. Hammond, J. Meyer, N. E. Widjonarko, P. N. Ndione, A. K. Sigdel, A. Garcia, A. Miedaner, M. T. Lloyd, A. Kahn, D. S. Ginley, J. J. Berry, D. C. Olson, *J. Mater. Chem.* **2012**, *22*, 3249.

[14] A. Garcia, G. C. Welch, E. L. Ratcliff, D. S. Ginley, G. C. Bazan, D. C. Olson, *Adv. Mater.* **2012**, *24*, 5368.

[15] O. Wiranwetchayan, Z. Liang, Q. Zhang, G. Cao, P. Singjai, *Mater. Sci. Appl.* **2011**, *2*, 1697.

[16] M. T. Lloyd, C. H. Peters, A. Garcia, I. V. Kauvar, J. J. Berry, N. O. Reese, M. D. McGehee, D. S. Ginley, D. C. Olson, *Sol. Energy Mater. Sol. Cells* **2011**, *95*, 1382.

[17] E. Voroshazi, B. Verreet, A. Buri, R. Müller, D. Di Nuzzo, P. Heremans, *Org. Electron.* **2011**, *12*, 736.

[18] E. L. Ratcliff, J. Meyer, K. X. Steirer, A. Garcia, J. J. Berry, D. S. Ginley, D. C. Olson, A. Kahn, N. R. Armstrong, *Chem. Mater.* **2011**, *23*, 4988.

[19] K. X. Steirer, P. F. Ndione, N. E. Widjonarko, M. T Lloyd, J. Meyer, E. L. Ratcliff, A. Kahn, N. R. Armstrong, C. J. Curtis, D. S. Ginley, J. J. Berry, D. C. Olson, *Adv. Energy Mater.* **2011**, *1*, 813.

[20] K. X. Steirer, J. P. Chesin, N. E. Widjonarko, J. J. Berry, A. Miedaner, D. S. Ginley, D. C. Olson, *Org. Electron.* **2010**, *11*, 1414.

[21] M. Kröger, S. Hamwi, J. Meyer, T. Riedl, W. Kowalsky, A. Kahn, *Org. Electron.* **2009**, *10*, 932.

[22] M. Kröger, S. Hamwi, J. Meyer, T. Riedl, W. Kowalsky, A. Kahn, *Appl. Phys. Lett.* **2009**, *95*, 123301.

[23] J. Meyer, A. Kahn, *J. Photon. Energy* **2011**, *1*, 011109.

[24] S. Hamwi, J. Meyer, M. Kröger, T. Winkler, M. Witte, T. Riedl, W. Kowalsky, A. Kahn, W. Kowalsky, *Adv. Funct. Mater.* **2010**, *20*, 123301.

[25] M. T. Greiner, M. G. Helander, W.-M. Tang, Z.-B. Wang, J. Qiu, Z.-H. Lu, *Nat. Mater.* **2012**, *11*, 76.

[26] J. Meyer, S. Hamwi, M. Kröger, W. Kowalsky, T. Riedl, A. Kahn, *Adv. Mater.* **2012**, *24*, 5408.

[27] D. Cahen, A. Kahn, *Adv. Mater.* **2003**, *15*, 271.

[28] D. Cheyns, J. Poortmans, P. Heremans, C. Deibel, S. Verlak, B.P. Rand, J. Genoe, *Phys. Rev. B* **2008**, *77*, 165332.

[29] A. Wagenpfahl, D. Rauh, M. Binder, C. Deibel, V. Dyakonov, *Phys. Rev. B* **2010**, *82*, 115306.

[30] S. R. Cowan, W. L. Leong, N. Banerji, G. Dennler, A. J. Heeger, *Adv. Funct. Mater.* **2011**, *21*, 3083.